An edited version of this paper was published by AGU.

The potential of QuikSCAT and WindSat observations for the estimation of sea surface wind vector under severe weather conditions

Y. Quilfen[1, *], C. Prigent[2], B. Chapron[1], A. A. Mouche[1], N. Houti[2]

[1] Laboratoire d'Océanographie Spatiale, IFREMER, Plouzané, France
[2] Laboratoire d'Etude du Rayonnement et de la Matière en Astrophysique, Observatoire de Paris, Paris, France

*: Corresponding author : Quilfen Y., email address : Yves.Quilfen@ifremer.fr

Abstract:

The physics of remote sensing sea surface measurements is still poorly understood under severe weather conditions. Wind vector algorithms are usually developed for non-precipitating atmospheres and for wind speeds less than 20 m/s. In this study, we analyze observations from the QuikSCAT Ku-band scatterometer collocated with the WindSat full polarimetric microwave radiometer to estimate the potential of these two instruments for sea surface wind retrieval under severe weather conditions. The Jason altimeter provides independent measurements of wind speed and rain rate for comparison purposes. The sensitivity of the radar cross-sections and brightness temperatures to the wind speed and direction is directly studied from the observations and compared with semi empirical models. This study clearly demonstrates that wind vector retrieval under extreme condition is feasible. Comparisons between QuikSCAT and WindSat coincident observations evidence a better sensitivity of the active mode to low and moderate winds and more sensitivity to high wind speeds in the passive mode. Although the WindSat observations are affected by water vapor, cloud, and rain, especially at and above 18 GHz, the measurements are sensitive to wind speed even at high wind speeds. Contrarily to the active instrument, there is no saturation at high winds. The sensitivity clearly tends to increase for winds above 15 m/s. For the wind direction, the amplitude of the azimuthal modulation in the active mode decreases with increasing wind speed, while it increases for the passive measurements. The development of specific wind retrievals under severe weather conditions is encouraged and a simple illustration is provided.

Keywords: Radiometer, scatterometer, winds.

1. Introduction

No existing sensor has been specifically designed to probe the sea surface during extreme weather events and there is a need to elaborate from existing sensors. Already decided operational Earth observation missions for the coming 15 years include scatterometers (the Meteorological Operational, MetOp, satellite series) and microwave radiometers (the National Polar-Orbiting Operational Environmental Satellite System, NPOESS, and MetOp satellite series). A critical review of the scatterometer and microwave radiometer potentialities / limitations to measure the surface winds under severe weather conditions is thus necessary. The sensitivity of the various instruments to the extreme events has to be objectively analyzed, under the same conditions, i.e., when coincident observations of both instruments are available. This can further lead to potential synergies between active and passive measurements on future Earth observation missions. The recent satellite polarimetric measurements from WindSat (Gaiser et al., 2004), launched in January 2003 have not been completely explored yet and provide new information under high wind speed and / or intense rain.

The physics of remote sensing measurements over sea surface is still poorly understood under extreme conditions. Remote sensing at high wind speed is mostly controlled by the observation ability to directly or indirectly probe the wave breaking impacts. The wind vector algorithms are usually developed for non-precipitating atmospheres and for wind speeds less than 20 m/s. Preliminary evaluations of the first versions of the ocean wind algorithms from WindSat under hurricane conditions (Adams et al., 2006) concluded that the wind speed was strongly affected by heavy clouds and precipitation. However, these results were only obtained after less than 3 years of

70 WindSat operation and full use of the polarimetric information combined to innovative

71 approaches should improve the retrievals (Adams et al., 2006). Concerning active

72 measurements, the larger wave breaking signatures as well as foam and bubble impacts

73 on the ocean surface dielectric and geometrical properties have been analyzed with

74 altimeter measurements (Quilfen et al., 2006). At larger incidence angles provided by

75 scatterometer observations, larger wave breakings can provide a very active source to

76 generate shorter scale roughness (Kudryavtsev and Johannessen, 2004) to help maintain

77 the wind speed sensitivity. Larger wave breaking events correspond to larger zones

78 covered with foam. More interestingly, larger breakers are associated with thicker foam

79 patches (Reul and Chapron, 2003). These two aspects (coverage and thickness) have

80 significant impacts on passive radiometric measurements.

81 In this study, we analyze multi-sensor observations from the QuikSCAT Ku-band

82 scatterometer collocated with the WindSat full polarimetric microwave radiometer. The

83 Jason altimeter mission provides independent measurements of wind speed, rain rate, and

84 atmospheric water content to help interpret the results. A systematic data screening tool

85 has been developed to collocate the three different sensors within a given space / time

86 window. The data are presented in section 2, with special focus on the rain flagging

87 procedure. In section 3, the sensitivity of the radar cross-section and brightness

88 temperatures to the wind speed and direction is studied from the observations and

89 compared with semi-empirical model simulations, with emphasis on the high wind speed

90 regime and on the effect of the atmospheric conditions. In section 4, the nominal wind

91 vector retrievals from both WindSat and QuikSCAT are compared and presented to

92 highlight the possible residual errors in the WindSat wind vector retrieval. Finally, in

93 section 5, retrievals using various observation combinations are tested, using both the

94 radiometer and the scatterometer, to help analyze the information content of passive and

95 active observations, and to show that the WindSat nominal wind speed retrieval can be

96 improved to provide valuable estimates as well as to complement the radar measurements

97 under severe weather conditions.

98

99 **2. Data**

100 **2.1. The instrument characteristics**

101 **2.1.1. WindSat**

102 Coriolis is a 3-year demonstration / validation mission sponsored by the Department of

103 Defense Space Test Program, the U.S. Navy, and the National Polar-Orbiting Operational

104 Environmental Satellite System (NPOESS) Integrated Program Office. It was launched

105 on January 6, 2003, on a geosynchronous polar orbit, with ascending node at 17:59 UTC.

106 WindSat onboard the Coriolis mission is a polarimetric microwave radiometer developed

107 and built by the Naval Research Laboratory (NRL). Its objective is to demonstrate the

108 potential of polarimetric measurements to estimate the ocean surface wind vector (speed

109 and direction).

110 The measurement principle makes use of the natural microwave emission of the sea

111 surface that varies with sea surface roughness. The rougher the sea, the more intense is

112 the emission. The received energy is a combination of energy emitted from the ocean

113 surface, from the atmosphere, and from the atmosphere reflected off the surface. WindSat

114 is the first space borne polarimetric microwave radiometer. It measures not only the

115 orthogonal polarizations (vertical and horizontal), but also the cross-correlation of the

116   vertical and horizontal polarizations. The cross-correlation terms represent the third and

117   fourth parameters of the modified Stokes vector (U and F). The Stokes vector provides a

118   full characterization of the electromagnetic signature of the ocean surface, and the

119   independent information needed to determine the wind direction.

120   WindSat uses a 1.8-m offset reflector antenna fed by eleven dual-polarized feed horns.

121   It operates at 6.8, 10.7, 18.7, 23.8, and 37 GHz, with 10.7, 18.7, and 37 GHz fully

122   polarimetric (the four Stokes parameters are measured, V, H, U, and F) whereas the other

123   channels are only measured in the two orthogonal polarizations (V and H). The Earth

124   incidence angle is close to 53° (respectively 53.5°, 49.9°, 55.3°, 53.0° and 53.0° for each

125   frequency) and the spatial resolution ranges from 40 km x 60 km at 6.8 GHz to 8 km x 13

126   km at 37.0 GHz. The expected accuracy is 0.75 K for the V and H channels and 0.25 K

127   for the third and fourth Stokes parameters. A complete description of the instrument and

128   its characteristics is given in Gaiser et al. (2004).

129

130   **2.1.2. QuikSCAT**

131   The SeaWinds instrument on QuikSCAT is an active microwave radar designed to

132   measure the electromagnetic backscatter from the wind roughened ocean surface. The

133   SeaWinds instrument uses a rotating dish antenna with two spot beams that conically

134   sweep, producing a circular pattern on the surface. The antenna radiates microwave

135   pulses at a frequency of 13.4 GHz. The antenna spins at a rate of 18 rpm, scanning two

136   pencil-beam footprint paths at incidence angles of 46° (H-pol) and 54° (V-pol). The

137   instrument collects data over ocean, land, and ice in a continuous, 1,800 km wide band

138   centred on the spacecraft nadir ground track, covering 90% of Earth's surface each day.

139   Spaceborne scatterometers transmit microwave pulses to the ocean surface and

140   measure the backscattered power received at the instrument. Since atmospheric motions

141   themselves do not substantially affect the radiation emitted and received by the radar,

142   scatterometers use an indirect technique to measure wind velocity over the ocean. Wind

143   over the ocean generates ripples and small waves, which roughen the sea surface. These

144   waves modify the radar cross-section (σ_o) of the ocean surface and hence the magnitude

145   of backscattered power. In order to extract wind velocity from these measurements, a

146   relationship between σ_o and near-surface winds, known as the geophysical model

147   function, has to be established.

148   **2.2. The collocation methodology and criteria**

149   The "Centre ERS d'Archivage et de Traitement" (CERSAT) located at the "Institut

150   Français de Recherche pour l'Exploitation de la Mer" (IFREMER, France) is a mirror site

151   for the QuikSCAT data and thus manages the archive of levels 2A and 2B products for

152   the complete QuikSCAT mission. CERSAT also archives the data from all scatterometer

153   missions and most of the altimeter missions. The WindSat product version used for

154   collocation with QuikSCAT and Jason is the last one delivered in 2006, version 1.9. At

155   the end of July 2006, the SeaWinds project began producing QuikSCAT data to replace

156   version 2.4, using new processing software that features an improved rain flag, a better

157   performance at high wind speeds, and a 12.5 km wind vector retrievals for level 2 data.

158   This improved data set is used in the present study.

159

160   CERSAT produced the WindSat / QuikSCAT and the WindSat / Jason collocated data

161   set for the complete available WindSat data set, covering February 2003 to November

162   2005 with gaps. Sensors are collocated by pairs, WindSat with QuikSCAT and WindSat

163   with Jason. The data from two sensors are collocated when the time difference is less

164   than one hour and when their ground distance is less than 25 km. All parameters from the

165   L2A (products containing instrumental data among which the radar cross-sections), L2B

166   (products containing geophysical data, i.e., wind vector), SDR (products containing

167   instrumental data among which the brightness temperatures), EDR (products containing

168   geophysical data, i.e., wind vector and atmospheric parameters), or GDR (products

169   containing both low level and geophysical data, i.e., wind vector, radar cross-sections)

170   products are included in the collocated product, depending on which sensors are

171   concerned. For this study, we use two months (February-March 2003) of WindSat /

172   QuikSCAT collocated data for the analysis of the lower level data (radar cross-section

173   and brightness temperature) and four months (February-May 2003) for the analysis of the

174   wind data. Fifteen months (February 2003 - April 2004) of WindSat / Jason collocated

175   data are also examined for comparisons.

176

177   **2.3. The rain flag issue**

178   Rain effects on passive and active microwave measurements depend on the sensing

179   frequency and on the sensor measurement geometry. It has been shown (Tournadre and

180   Quilfen, 2003) that the Ku-band QuikSCAT data are affected even by moderate rain rate.

181   Measurements of the ocean surface σ_0 become contaminated for several reasons. Some of

182   the transmitted energy is scattered back towards the scatterometer by the rain and never

183   reaches the ocean surface. Energy backscattered from rain can constitute a significant

184   portion of the measured echo energy. Some of the transmitted energy is scattered and / or

185 absorbed by the rain and is never measured by the scatterometer. This has the effect of

186 attenuating the echo energy from the ocean. Additionally, the rain roughens the ocean

187 surface and changes its radar cross-section. The total effect results in overestimation of

188 the lower winds and underestimation of the higher winds (Tournadre and Quilfen, 2003).

189 Two rain flags are included in the QuikSCAT Level 2B data to indicate detection of rain

190 contamination. The mp_rain_probability is derived using the Impact-based

191 Multidimensional Histogram (IMUDH) rain-flagging technique developed by Huddelston

192 and Stiles at NASA JPL (2000). Briefly, mp_rain_probability from IMUDH does not flag

193 a specific rain rate but a likelihood that the wind speed is perturbed by more than 2 m/s or

194 the direction by more than 15°. The nof_rain_index is derived using the Normalized

195 Objective Function (NOF) rain-flagging technique developed by Mears (2000). It is

196 based upon a simplified version of the standard model function to determine a maximum

197 likelihood estimator and a wind speed for each wind vector cell. In the present study, we

198 use the mp_rain_probability (hereafter RP) since it was shown more efficient (Freilich

199 and Vanhoff, 2006). A threshold of 0.2 for the QuikSCAT RP rain flag is a good

200 compromise to flag the rain-contaminated QuikSCAT data and to avoid QuikSCAT high

201 wind over-flagging (Tournadre and Quilfen, 2005).

202 The WindSat rain flag provided in the EDR products is used in the study. It is based

203 upon a threshold of the 0.2 mm value for the Cloud Liquid Water content (hereafter

204 CLW). An illustration of the rain flagging problem is provided in Figure 1. Indeed, as

205 discussed in Tournadre and Quilfen (2005) using the precipitation radar data from the

206 Tropical Rainfall Measuring Mission (TRMM), the RP rain flag is not self sufficient

207 under high wind conditions. Due to WindSat / QuikSCAT time and space collocation

208 errors and high time and space rain cell variability, the WindSat CLW test may fail also

209 to flag the QuikSCAT rain-contaminated data. Figure 1 displays the QuikSCAT wind

210 speed as a function of the RP and CLW parameters (left) and the number of points in

211 each RP / CLW bin (right). The two RP and CLW thresholds used for rain flagging are

212 indicated. High values of RP are associated with mean high winds as measured by

213 QuikSCAT. For RP values larger than about 0.8 the CLW content is greater than 0.2 mm,

214 meaning that these points are clearly associated with rain in stormy conditions and

215 detected by the two flags. Data with RP values between 0.2 and 0.8 and CLW values

216 lower than 0.2 may be associated either to RP over-flagging or to CLW under-flagging.

217 Accounting for the high space / time variability of rain events, possible CLW under-

218 flagging may be due to the space / time difference between the QuikSCAT and WindSat

219 measurements. Figure 1 (right) shows that for about 6% of the points the QuikSCAT flag

220 is not set when the WindSat one is. It is impossible to distinguish between WindSat over-

221 flagging due to space / time collocation errors and QuikSCAT under-flagging. The higher

222 CLW values associated with mean high QuikSCAT winds could be both. For this reason

223 and because both instruments are affected by rain, the two flags are often used jointly in

224 the study: it corresponds to discard 8.3% of the collocated data.

225

226 **2.4. Statistics of the winds in the collocated database**

227   Figure 2 illustrates the spatial distribution of the collocated WindSat / QuikSCAT and

228 WindSat / Jason observations. The WindSat / QuikSCAT collocated database covers

229 most of the ocean with a larger concentration of match-ups at tropical and sub-tropical

230 latitudes than at high latitudes where higher wind speeds are expected. Inversely, the

231 WindSat / Jason database covers mainly the high latitudes in southern oceans. This is

232 inherent to the sensor geometries and orbital configuration. As a consequence, the results

233 obtained in this study should be carefully analyzed with respect to these non uniform

234 geographical distributions.

235   Figure 3 (top) shows the distribution of the QuikSCAT and WindSat retrieved wind

236 speed and direction for the collocated database, along with the National Centers for

237 Environmental Prediction (NCEP) model results (these histograms include only the pixels

238 for which the WindSat wind speeds are estimated, i.e., excluding the rainy pixels). As

239 expected, the wind speed distribution peaks around 7 m/s, with limited match-ups above

240 15 m/s, regardless of the wind information sources. The wind direction with respect to the

241 North has two peaks, a large one around 270° (easterly winds) and a weaker one around

242 90° (westerly winds). The bottom panels on Figure 3 zoom on the high wind tail of the

243 distribution and show that westerlies dominate for high wind speeds. The population of

244 high wind speed retrieved by QuikSCAT is lower than the one estimated from the other

245 sources.

246

247 **3. Sensitivity of the passive and active measurements to the surface wind**

248 **and comparison with semi-empirical models**

249   The sensitivities of the active and passive instruments to the wind vector are analyzed

250 from the satellite observations and compared with semi-empirical models. In this section,

251 only the non-rainy observations are considered, as flagged from both QuikSCAT and

252 WindSat (pixels declared rainy by QuikSCAT or WindSat are not considered).

253

254

3.1. The active responses

Asymptotic models (small perturbation and small slope approximation at first order, Kirchoff approximation or two-scale model) used to predict the normalized radar cross-section of the sea surface generally fail to reproduce in details backscatter radar measurements. In particular, the predicted polarization ratio versus incidence angle and azimuth angle is not in agreement with experimental data. This denotes the inability of the standard models to fully take into account the roughness properties with respect to the sensor configuration (frequency, incidence, and polarization).

One of the models (Mouche et al., 2007a) used in this study considers the latest improvements obtained in the field of approximate scattering theories of random rough surfaces using the local and resonant curvature approximations (RCA). The RCA model is based on an extension of the Kirchoff approximation up to first order to relate explicitly the curvature properties of the sea surface to the polarization strength of the scattered electromagnetic field. As shown in Mouche et al. (2007a), dynamically taking into account the sea surface curvature properties is crucial to better interpret normalized radar cross-section and polarization ratio sensitivities to both sensor characteristics and geophysical environment conditions. The validation of the RCA model, presented in Mouche et al. (2007b), makes use of NSCAT Ku-band scatterometer data and aircraft C- and X-band data acquired during stormy conditions. It shows significant improvement obtained in modelling the polarization ratio with the RCA model as compared with the classical approaches.

276 The second model used to compare with QuikSCAT data assumes a decomposition for

277 the sea surface. Following Quilfen et al. (1999), Kudryavtsev et al. (2003) decomposed

278 the normalized radar cross section (σ_0) as a sum of two terms. The regular surface is

279 associated with the Bragg scattering theory whereas zones of enhanced roughness

280 associated to the presence of individual breakers contribute to the radar signal through

281 non polarized, scalar, contributions. The Bragg scattering theory is taken into account by

282 a two-scale model. Note that this model has also been developed to corroborate the

283 NSCAT data.

284 Figure 4 presents the comparison between the QuikSCAT normalized radar cross-

285 section σ_0 and those estimated using the RCA and Kudryavtsev models, as a function of

286 wind speed. σ_0 increases quickly with the wind speed at low to moderate winds, then

287 saturates with increasing wind speed. The RCA model indicates a full saturation, while

288 the data still show some sensitivity with increasing wind speed. The Kudryavtsev model

289 fits the data slightly better at high winds. Inclusion of enhanced roughness areas (linked

290 to breakers) in the surface description certainly helps increase the σ_0 sensitivity to high

291 winds. The modeled and measured polarization differences are in good agreement for

292 both models, although larger than shown in the data beyond 25 m/s for the Kudryavtsev

293 model. It decreases with increasing wind speed from moderate to about 20 m/s, because

294 the HH polarization shows slightly better sensitivity with increasing winds. The

295 Kudryavtsev model reproduces the crossing of the HH (46° incidence angle) and VV (54°

296 incidence angle) curves near 20 m/s. Faster decreasing sensitivity of the σ_0 VV with

297 increasing wind speed beyond 25 m/s was also found by Fernandez et al. (2006) using

298 airborne scatterometer and radiometer data during tropical cyclone events. They

299   measured approximately a 4 dB (2 dB) σ_0 increase at HH (VV) for winds increasing

300   from 25 to 60 m/s.

301   The dependence of the mean σ_0 on the wind direction is shown in Figure 5, for VV

302   (top panel) and HH (bottom panel) polarizations, for the RCA model (blue curves) and

303   the data (red curves), at 6, 14, and 22 m/s. Only the RCA model results are presented for

304   the anisotropic part because the Kudryavtsev model in its present form does not account

305   for a wind speed dependence of the azimuthal modulation. The data and the RCA model

306   are in relative good agreement at HH polarization, but the amplitudes of the azimuthal

307   modulation differ significantly at VV polarization. The RCA model indicates dramatic

308   increase of the modulation with increasing wind speed while data feature slightly

309   decreasing modulation. This is also true at HH polarization, but to a smaller extent. Such

310   apparent discrepancies are mainly due to the statistical surface description used to

311   compute the RCA predictions. Adjustments could certainly be made but are beyond the

312   scope of this study. RCA predicts larger HH cross-section than any other asymptotic

313   scattering model and fits the measurements better. Moreover, the RCA model tends

314   towards a Kirchoff asymptotic relation at high winds, i.e. the sea surface polarization

315   sensitivity strongly decreases. At the extreme, both VV and HH predictions match.

316   Careful analysis shall be directed to data showing larger HH measurements than VV

317   ones. Indeed, this necessarily indicates distinct scattering mechanisms to be possibly

318   attributed to breaking event effects.

319

320

321

3.2. The passive responses

The passive microwave observations are sensitive to the sea surface as well as to the atmosphere. To quantify the brightness temperature (Tb) behaviour, we computed their mean values averaged into wind speed bins and for three different integrated water vapor (WV) ranges. This is illustrated in Figures 6 and 7. Only the three lower frequencies are described in these figures since they are less affected by the atmosphere. The behaviour of all 5 frequencies will be described later in this section. Figure 6 displays the mean values using the WindSat / Jason database, where the wind speed reference is the ECMWF one and the WV reference is either the WindSat one (solid lines) or the Jason Microwave Radiometer one (JMR, dashed lines) for comparison purpose. Figure 7 displays the same features with the QuikSCAT wind speed and the WindSat WV values as references. It can be seen that the results agree very well when using indifferently the Jason or WindSat WV data and the QuikSCAT or ECMWF wind speed. The most striking feature is that the H polarization is more sensitive to the wind that the V polarization. The V polarization also appears related to the water vapor content, especially at 6.8 and 18.7 GHz. This is expected from the 18.7 GHz but not from the 6.8 GHz channel: the 6.8 GHz is actually sensitive to the sea surface (SST) temperature that is usually correlated with the integrated water vapor in the atmosphere. From RTTOV model simulations with a wind speed of 7m/s and for a typical tropical atmosphere, the change in Tb due to a SST increase of 1 K is of the order of 0.6K (resp. 0.4K) at 6 GHz for the V polarization (resp. H). It is twice less at 18 GHz and keeps decreasing with frequency. Most of the high WV content data are associated with moderate winds and the winds larger than 10 m/s are generally associated with low WV values. The H-pol Tb's

345   increase quickly with the wind speed and do not present any saturation at wind speed

346   greater than 20 m/s, whatever the WV range. There is roughly a 1K per 1 m/s slope,

347   slightly larger for winds above 12 m/s as it can be seen mainly at 6.8 and 10.7 GHz. This

348   change in the slope is much more pronounced in the V-pol data: the Tb's are not very

349   sensitive to wind speed increase from low to moderate winds. Indeed, at 53° incidence

350   angle (which is close to the Brewster angle for sea water in this frequency range), the V-

351   pol signal is not very sensitive to the surface roughness. The change in V-pol is

352   essentially due to the presence of foam that changed with wind speed. The foam coverage

353   increase with wind speed is exponential in shape in most models (e. g., Monahan and

354   O'Muircheartaigh, 1986), similar to the observed change in the V-pol signal with wind

355   speed. The V-pol wind speed sensitivity seems reduced in presence of high integrated

356   water vapor content. The 18.7 GHz channel is much more sensitive to the WV content

357   than to the wind speed, especially for V-pol with a difference of roughly 25 K at 10 m/s

358   between the two extreme WV ranges, while it is only 8 K at lower frequencies.

359   The WindSat / QuikSCAT database is our primary source for comparison between

360   passive and active measurements under severe weather conditions because it contains

361   more high wind speed observations. To further justify the use of QuikSCAT wind speed

362   as reference, rather than NCEP also available in the database, Figure 8 presents the

363   brightness temperature standard deviations (SD's) for wind speed bins, when QuikSCAT

364   and NCEP wind speeds are used as reference. A water vapor threshold of 20 mm has

365   been applied to minimize the atmospheric contribution to the Tb's variability. The SD's

366   values contain information on the variability of the other geophysical parameters (SST,

367   salinity, waves) into 2m/s bins but also contain information on the correlation between

368   the chosen reference wind speed and the brightness temperature. The lower the SD's, the

369   better the correlation between wind speed and Tb, the better the wind speed reference. It

370   can be seen that the SD's are generally lower when the satellite winds are used, for winds

371   beyond 10 m/s. The SD's increase with increasing channel frequency. The lowest SD's

372   obtained with the QuikSCAT winds justify the subsequent use of QuikSCAT for the

373   evaluation of the WindSat radiometric measurements.

374   Figure 9 illustrates the Tb's behavior as a function of wind speed for the five WindSat

375   channels. For comparison purposes, the sea surface emissivity model FASTEM-3

376   (English and Hewison, 1998; Deblonde, 2000) from the RTTOV fast radiative transfer

377   model has been used (Eyre, 1991; Matricardi et al., 2004). The development of the

378   RTTOV fast radiative transfer model is part of the EUMETSAT sponsored NWP-SAF

379   activities. The last RTTOV-8 version includes the capability to simulate polarimetric

380   radiometers (e.g., WindSat). In line with the semi-empirical model developed by

381   Kudryavtsev and his co-authors (2003), FASTEM-3 uses a two-scale ocean roughness

382   approximation and takes explicitly into account emissivity from foam patches. The ocean

383   permittivity is derived from Ellison et al. (1998) and the foam coverage calculated from

384   Monahan and O'Muircheartaigh (1986). The azimuthal dependence from Liu and Weng

385   (2002, 2003) is adopted in FASTEM-3, but with revised coefficients derived from the

386   model presented by Coppo et al. (1996) that predicts reduced amplitude of the azimuthal

387   dependence. Tb's have been computed for a dry (4 mm of water vapor content and a SST

388   of 10° C) and a wet (40 mm of water vapor content and a SST of 26° C) atmospheres.

389   From the WindSat observations, dry (wet) cases have been selected using measurements

390   for which the integrated water vapor content is in the 0 to 20 mm (20 to 60 mm) range,

391   and the distribution has been adjusted in order to obtain a mean SST of 10° C and 26° C

392   for the dry and wet atmospheres, respectively. The general agreement between WindSat

393   and RTTOV is good, although the mean Tb difference for the two water vapor ranges is

394   generally greater for RTTOV, as expected by the fact that the selected atmospheres for

395   the simulations corresponds to extreme cases, especially for the dry atmosphere.

396   However, the sensitivity to the wind speed is well reproduced although there is a faster

397   increase in H-pol at high wind speeds for the model simulation. This difference is channel

398   dependent and is larger at lower frequencies. As previously noted, the model confirms

399   that there is no saturation of the brightness temperatures at high wind speeds. There are

400   few data beyond 25 m/s, but the RTTOV model indicates continuous increase in Tb's

401   beyond 30 m/s. This is exclusively due to the foam coverage parameterization, i.e,

402   Monahan and O'Muircheartaigh (1986), and may certainly be questioned, e.g., the foam

403   coverage percentage exceeds 100% beyond 40 m/s. It may explain the faster increase of

404   the H-pol RTTOV simulations by comparison with data.

405   The 3rd (U) and 4th (F) Stokes parameters are computed for the 10.7, 18.7, and 37.0

406   GHz channels. Sensitivity of these parameters to the wind direction has been quantified

407   (Yueh et al., 2006). Figures 10 and 11 further illustrate this sensitivity in case of a dry

408   (Figure 10) and a wet (Figure 11) atmospheres as selected from the data to outline that

409   these parameters are little affected by the atmosphere contrarily to the two first Stokes

410   parameters. The azimuthal modulation increases with wind speed up to 18 m/s and does

411   not vary significantly for winds beyond 20 m/s (red curves). Still, the scarcity of high

412   wind data does not enable confident estimates of the modulation intensity. A small phase

413   shift is apparent in the signal as the wind speed increases, already noted in Yueh et al.

414   (2006). The maximum amplitude of 4 K (U) and about 0.7 K (F) at 18.7 GHz for wind

415   speed higher than 16 m/s is consistent with the Yueh et al. results. As expected, the 1st

416   harmonic dominates in the U modulation, with decreasing 2nd harmonic modulation with

417   increasing frequency, while the 2nd harmonic is predominant in the F modulation. The F

418   signal is less than 0.2 K at 37.0 GHz and is almost unusable. U thus exhibits a strong

419   upwind / downwind modulation while F exhibits a strong upwind / crosswind

420   modulation.

421   The azimuthal modulation remains almost unchanged in case of a wet atmosphere

422   (Figure 11) although its amplitude slightly decreases. Sensitivity of the U and F Stokes

423   parameters to the wind direction is not affected by atmospheric contribution, even at 37

424   GHz. From aircraft observations with the WINDRAD instrument (17, 19, and 37 GHz),

425   Yueh et al. (2006) also observed that the radiometric wind direction information was

426   robust to weather conditions, with similar response from 17 to 37 GHz, even at wind

427   speed above 20 m/s.

428   Figure 12 presents a comparison between WindSat and the azimuthal modulation from

429   the RTTOV model. The model reproduces quite well the azimuthal modulation but shows

430   also systematic differences with the WindSat data. It features much larger amplitudes for

431   F. It predicts an increase of the modulation from low to high winds in agreement with

432   data for U but this increase is not present in the data for F. For F, the RTTOV model

433   modulation is almost the same regardless of the channel whereas the data show much

434   weaker modulation at 37 GHz. For U, the RTTOV model modulation is decreasing with

435   increasing frequency whereas the data show nearly constant azimuthal modulation

436   amplitude. The distribution of the first and second harmonics is comparable for F for

437   which the upwind / crosswind modulation dominates for both model and data. It differs

438   for U for which the data show increasing (decreasing) upwind / downwind (upwind /

439   crosswind) modulation with increasing frequency whereas RTTOV has the opposite

440   behavior. Finally, but not surprisingly, the disagreement is larger for higher winds for

441   which there are significant differences in the amplitude and phase of model and data

442   azimuthal modulations.

443   **3.3 Discussion**

444   It is worth reminding that physical models are generally developed to account for

445   mechanisms taking place under average weather conditions. It is thus not surprising that

446   extrapolation to severe weather conditions does not compare very well with data.

447   However, the good agreements obtained in the mean behavior of the simulations, for both

448   active and passive modes, are stimulating to pursue efforts in the physical modeling field.

449   Note that the RCA model is developed in a way that enables its extension to passive

450   measurements. Such a synthetic tool will help better analyze the active / passive

451   measurements, with a consistent approach under extreme weather conditions.

452   Under high wind conditions, the sea surface is no longer simply related to the wind

453   speed. In winds approaching hurricane strength, an enhanced breaking activity is taking

454   place at the surface of the ocean. Both whitecaps and spray droplets proliferate, as well as

455   intense mixing of the surface waters with turbulent transport of bubbles to depth.

456   Whitecap bubbles and sea spray provide additional surfaces and volumes that may impact

457   the transfer of any quantity normally exchanged at the air–sea interface. The key

458   parameterization to describe the ocean surface dynamics under such extreme conditions is

459   the distribution of the total length of breaking fronts moving with a given speed or having

460 a certain wavelength scale. As it can be expected, under extreme wind forcing, breaking

461 waves are distributed over a wider range of surface wave scales as compared to more

462 gentle conditions. As larger waves are involved in breaking processes, both foam

463 coverage and foam thickness significantly increase with increasing wind speeds (Reul

464 and Chapron, 2003). This is certainly the main principle leading to passive measurement

465 sensitivities to high wind conditions. Further, spume drops torn off breaking crests are

466 sprayed inside the air flow at higher height, i.e., the larger scale mean height, to possibly

467 significantly affect the turbulent mixing. This latter effect can then lead to acceleration of

468 the air flow and reduction of the surface drag, as suggested by recent wind profiles

469 measurements under hurricane wind conditions (Powell et al., 2003). Consequently,

470 ocean surface passive remote sensing measurements at very high wind speeds are

471 certainly well adapted and mostly controlled by the instrument abilities to directly or

472 indirectly probe the larger wave breaking impacts. Emissivity models as well as

473 measurements predict saturation in foam emissivity, i.e., foam approaches the behaviour

474 of a black body, for sea-foam thickness larger than about 2 times the electromagnetic

475 wavelength (Rose et al., 2002; Reul and Chapron, 2003). Passive measurements below 15

476 GHz, and to lesser extent at higher frequencies, are thus expected to provide interesting

477 measurements under very high wind speeds (> 30 m/s). This is confirmed by the WindSat

478 measurements. Concerning active measurements, these larger wave breaking signatures

479 as well as foam and bubble impact on the ocean surface dielectric properties have

480 apparently been successfully captured with altimeter measurements (Quilfen et al., 2006).

481 At low incidence angle, large wave geometry can indeed contribute to the signal

482 sensitivity. At backscatter geometry with larger incidence angle, larger wave breakings

483   have indirect effects to provide a very active source to generate shorter scale roughness

484   (Kudryavtsev and Johannessen, 2004), and thus to maintain the sensitivity of the radar

485   cross-section to wind speed as shown in Figure 3 for the Kudryavstev semi-empirical

486   scattering model. This source may thus somehow compensate the plausible reduction of

487   small scales direct wind generation, associated to the predicted surface drag reduction.

488   Furthermore, sharply crested waves can also directly enhance the mean backscatter

489   measurements, e.g., increasing radar sea spikes. Following these considerations,

490   backscatter measurements will not be fully saturated at very high wind speeds, as

491   confirmed from QuikSCAT or aircraft radar measurements (Fernandez et al., 2006).

492   However, in such a configuration, measurements shall be made at higher incidence,

493   possibly in horizontal polarization. The electromagnetic wavelength choice is not

494   expected to be crucial under extreme conditions to efficiently probe the ocean surface. To

495   avoid precipitation effects, measurements at lower frequencies (C- and L-bands) should

496   be considered. Finally, as the ocean surface is expected to exhibit localized and

497   intermittent processes, both passive and active estimates should not solely rely on the

498   mean instrumental measurement levels. To better characterize the expected randomness

499   of the fluctuating measurements under hurricane conditions, attention could also focus on

500   the higher order statistics, in particular the variance of the measured signals. Fluctuations

501   of both brightness temperatures and radar cross-sections inside stormy area have

502   generally been reported to vary a lot, with the normalized variance of the signals

503   increasing with wind speeds.

504   Comparisons between QuikSCAT and WindSat sensitivity to the wind speed evidence

505   a better sensitivity of the active mode to low and medium winds and more sensitivity to

506   high wind speed in the passive mode. QuikSCAT sensitivity to winds beyond 20 m/s, as

507   verified from few field experiments (Fernandez et al., 2006), is low and estimation of

508   extreme events intensity is thus difficult. On the other hand, this study illustrates the very

509   good sensitivity of WindSat to high winds, as also observed from the nadir viewing

510   Stepped Frequency Microwave Radiometer, SFMR (Fernandez et al., 2006). However,

511   WindSat being sensitive to surface temperature at low frequencies and to water vapor,

512   clouds and rain at higher frequencies, these variables have to be estimated separately.

513   Measurements from channel combinations have certainly to be used to extract the wind

514   information from these passive microwave observations.

515

516   4. Analysis of the retrieved WindSat and QuikSCAT wind vector

517   In this section, the WindSat and QuikSCAT wind retrievals from the operational

518   algorithms are compared, with special focus on the estimates under extreme weather

519   conditions.

520   4.1. Wind speed comparison

521   Figure 13 presents the distribution of the WindSat minus QuikSCAT wind speed

522   differences for non-rainy pixels. The mean WindSat minus QuikSCAT difference is 0.26

523   m/s and the standard deviation 0.89 m/s, with maximum and minimum values of 32 m/s

524   and -16 m/s, respectively. Figure 13 middle and bottom panels show the WindSat and

525   QuikSCAT wind speed distribution, respectively, for data for which the absolute value of

526   the wind speed difference is greater than 8 m/s. While the distribution of the QuikSCAT

527   wind speed is close the global mean wind speed distribution, the corresponding WindSat

528   distribution is shifted towards high wind speed values. It corresponds mostly to WindSat

529   wind speed overestimation due to atmospheric effects as already outlined in Freilich and

530   Vanhoff (2006). These data are filtered out for subsequent analysis. The new mean

531   difference and standard deviations are 0.25 m/s and 0.79 m/s, respectively.

532   Mean WindSat speeds binned by QuikSCAT wind speeds are presented in Figure 14,

533   for different WV content intervals. Data are filtered out for rain and for absolute wind

534   speed difference larger than 8 m/s. The results are quite similar with those obtained in

535   Freilich and Vanhoff (2006), although they did not analyze the effect of water vapor

536   content and used an older version of the WindSat products (NESDIS0). They also found

537   WindSat underestimation of high winds by a larger amount. Figure 14 shows that

538   WindSat winds are lower than QuikSCAT in clear sky and high wind conditions and

539   higher than QuikSCAT winds beyond 15 m/s in presence of high water vapor content.

540   The dependence of the comparison on WV may be interpreted as a residual error of the

541   WindSat winds due to multi-parameter retrieval algorithm errors in high winds and water

542   vapor content conditions. For the wind speed range below 15 m/s, good agreement is

543   found between QuikSCAT and WindSat.

544   Another validation is performed and illustrated in Figure 15 using the Jason and

545   ECMWF winds available using the WindSat / Jason collocated data set. Results are

546   slightly different from those obtained with the QuikSCAT comparison. We find a good

547   agreement between WindSat and Jason or ECMWF wind speed whatever the wind speed

548   range in clear sky conditions, although WindSat winds are slightly higher than the two

549   other wind sources. The dependency of the observed wind speed difference on increasing

550   water vapor is still apparent although less clear because there are few measurements

551   beyond 15 m/s wind speed and 20 mm integrated water vapor. Indeed the collocated

552   WindSat / Jason measurements are found mainly in mid-latitudes while the collocated

553   WindSat / QuikSCAT measurements are essentially found in tropical areas (Figure 2).

554   To conclude, good agreement is found between the WindSat and the QuikSCAT /

555   Jason / ECMWF winds, except for winds greater than about 17 m/s for which WindSat

556   winds are apparently lower than QuikSCAT winds. A residual dependency of the

557   WindSat winds on the water vapor appears for winds beyond 15 m/s.

558   **4.2. Wind direction comparison**

559   Figure 16, from top to bottom, presents the standard deviation of the difference

560   between the WindSat wind direction and the QuikSCAT, NCEP, and ECMWF wind

561   direction, respectively. Standard deviations (hereafter SD) have been computed for

562   different WV ranges and separately for the tropical and mid-latitude areas in order to

563   account for the mean SST variability. Data for which the direction difference is greater

564   than ninety degrees are discarded before estimation of the SD values. The comparison

565   with the three different data sources shows that the wind direction SD is greater for mid-

566   latitudes. It can be mainly explained as the result of the larger space / time variability in

567   mid-latitude areas, thus associated with larger collocation errors. The SD is larger than

568   20° at low wind speeds and decreases quickly with increasing wind speed to reach values

569   lower than 10°. SDs computed with QuikSCAT winds decrease faster which denotes the

570   higher QuikSCAT wind direction accuracy for medium winds. The comparison with

571   ECMWF provides still decreasing SD's for increasing wind speed beyond 15 m/s while

572   comparison with QuikSCAT and NCEP shows slightly increasing SD values. It must be

573   noted that there are few ECMWF wind speed data beyond 20 m/s. The comparison

574   between the three data sources show that the SDs are lower than 10° for winds from 10

575   m/s to 20 m/s. This is an excellent agreement, better than the previous WindSat accuracy

576   estimates that were of the order of 15° in this wind speed range using the former version

577   (NESDIS0) of the WindSat products (Monaldo, 2006; Freilich and Vanhoff, 2006).

578   WindSat version 1.9 product are thus a significantly improved over the former ones.

579   The comparison between QuikSCAT and NCEP shows the effect of WV on the wind

580   direction retrieval accuracy, as for the wind speed analysis. This effect is not clear in the

581   comparison with ECMWF. This is attributed to the different WindSat / QuikSCAT and

582   WindSat / Jason sampling (Figure 2). Although WindSat polarimetric measurements are

583   not much affected statistically by the atmosphere, as shown in Figure 11, the higher

584   scatter observed for higher water vapor content is certainly associated with the low signal

585   to noise ratio for polarimetric measurements. Indeed the azimuthal signal is of the order

586   of a few Kelvin. It is also not surprising that the mean SST conditions influence the

587   magnitude of the scatter to induce differences in the comparison between WindSat and

588   QuikSCAT, and WindSat and Jason measurements. Moreover, any error in the estimation

589   of one of the other parameters (wind speed, WV, SST) will affect the wind direction

590   retrieval of the multi-parameter retrieval process.

591   Figure 17 illustrates the difficulty of WindSat wind vector retrieval under stormy

592   conditions. The top left (right) panel gives the rain free QuikSCAT (WindSat) wind field

593   using the standard rain flag for each product. The bottom left (right) panel gives the

594   WindSat integrated water vapor content (rain rate). The 0.2 mm threshold on the cloud

595   liquid water content eliminates large interesting parts of the storm in the WindSat

596   estimates. Despite this severe screening, there are still pixels with anomalous wind speed

597   values on the south side of the storm. WV is equal or greater than 50 mm over the

598   displayed area. Wind vector retrieval under stormy conditions thus remains a challenge.

599

600   **5. Statistical analysis of the information content of the satellite**

601   **observations for surface wind retrieval under extreme conditions**

602   Different algorithms have been developed to retrieve the wind speed and direction

603   from the WindSat observations, ranging from physical models based on simulations to

604   purely statistical schemes relying on collocations with buoys. All the channels are not

605   systematically used. For instance, Bettenhausen et al. (2006) used a two step variational

606   estimation coupled to an efficient forward physical model to estimate first the wind

607   speed, the water vapor and liquid columns, and the surface temperature, and then the

608   wind direction. T_H at 6.8 GHz and T_F at 37 GHz are excluded. On the other hand, Brown

609   et al. (2006) developed an empirical wind vector retrieval scheme based on collocation

610   between QuikSCAT and WindSat.

611   In order to assess the potential of the passive and active microwave observations for

612   wind speed retrieval at high wind speeds, we attempt to reproduce the QuikSCAT wind

613   speed (assumed to be the reference wind speed) with different observation combinations.

614   A multi-linear regression algorithm is adopted. In a preliminary attempt, the training data

615   set used the natural wind speed distribution in the initial database (Figure 3). This

616   resulted in large biases in the retrieval of the high wind speed, due to the heavy weight of

617   wind speeds around 7m/s in this database. It was thus decided to weight the contribution

618   of the different wind speed to obtain the same proportion of all wind speed categories in

619   the database. The following results are obtained with this 'uniformed' database. For each

620   observation combination, the statistics of the difference with the expected winds are

621   calculated. They are a measure of the potential of this specific combination to retrieve

622   wind speed. These statistics are examined under high wind speed and rainy situations, in

623   order to assess the robustness of the retrieval under these conditions.

624   Figure 18 shows the results of the retrieved Windsat wind speed as compared to the

625   operational QuikSCAT wind speed (QuikSCAT wind speed minus the new estimated

626   wind speed) using 1) all the WindSat channels, 2) the WindSat channels without the 6.8

627   GHz, 3) WindSat without the 6.8 and 10.7 GHz channels, 4) all WindSat and QuikSCAT

628   observations together, 5) for comparison purposes, the wind speed provided in the

629   standard Windsat products. Table 1 gives the statistics of the estimates separating the

630   rainy and non-rainy cases, and the high wind speeds. Note that the statistics presented in

631   Figure 18 and in Table 1 are calculated on the original database, not on the 'uniformed'

632   database. As expected from the 'uniformed' database used for the training of the

633   algorithm, the performance of the retrieval is rather equivalent for all wind speed ranges.

634   The WindSat observations reproduce well the QuikSCAT wind speed up to 25 m/s.

635   Above 20 m/s, part of the discrepancy comes from the lack of high wind speed in the

636   database: although the database has been 'uniformed' for the training of the statistical

637   algorithm, at high wind speeds, the same samples are used many times, thus the

638   variability of the sample is not natural and might be unrealistic. However, it shows that

639   contrarily to the original algorithm that are tuned to be optimum for the most probable

640   winds (around 7 m/s), this simple algorithm performs well in the upper wind speed range,

641   above 15 m/s. Given that the observations are sensitive to the wind speed without

642   saturation to high wind, optimized algorithms designed for high wind speed conditions

643   can be developed and this little experiment proves it. Nevertheless, note that a residual

644   bias is observed for the most common winds around 7 m/s with the simple algorithm

645   developed here (overestimation of the retrieved wind as compared to the QuikSCAT

646   reference): it would be possible to develop different wind speed algorithms, depending

647   upon the wind speed ranges, based on a prior classification of the situations. From Figure

648   18, it appears that the 6 GHz channels do not provide significant additional information

649   (with or without these channels, the retrievals are very similar), but the 10 GHz channels

650   have a significant impact. Adding QuikSCAT to the WindSat observations does not

651   significantly change the results (note that if in Table 1 the rms is worse with QuikSCAT

652   than without it is related to the fact that the algorithm is not trained on the database that is

653   used to calculate the statistics, otherwise, adding information would make the statistic

654   similar or better).

656   **6. Conclusion and perspectives**

657   Under extreme weather conditions, accurate wind vector retrieval is difficult for four

658   main reasons. First, under high wind conditions, the sea surface is no longer simply

659   related to the wind speed. Breaking activity and associated whitecaps and spray taking

660   place at the surface of the ocean and interfere with the satellite response. There are

661   ongoing efforts to understand and model these complex effects. Second, both physical

662   models and wind vector retrieval methods have been primarily developed for medium

663   range wind conditions, that are much more common. Third, extreme weather conditions

664   are generally associated with clouds and rain that contaminate the satellite signal. The

665   impact of these perturbations increasing with increasing observation frequency. Freilich

666   and Vanhoff (2006) set the tone: 'Accurate wind retrievals are not possible at all in heavy

667   rain'. Not only the rain in the atmosphere absorbs and scatters the microwave response

668   but the rain drops on the ocean surface also affect the ocean roughness. Fourth, in high

669   wind conditions, the wind speed can vary greatly over the satellite footprint. Therefore,

670   the retrieval is really an average over the footprint and one often miss to measure the

671   extreme winds because of this smoothing effect.

672   However, this study shows that wind vector retrieval under extreme condition is

673   feasible. Comparisons between QuikSCAT and WindSat observations show that the

674   active mode is more sensitive to low and moderate winds whereas the passive mode

675   responds better to high wind speeds. Although the WindSat observations are affected by

676   water vapor, cloud, and rain, especially at and above 18 GHz, the measurements are

677   sensitive to wind speed even at high wind speed. Contrarily to the active instrument, there

678   is no saturation at high winds and the sensitivity clearly increases for winds above 20

679   m/s. Developments of wind retrieval from WindSat observations could thus certainly be

680   adapted to high wind speeds. As a first attempt, a multi-linear regression retrieval is

681   presented in this study to show consistent and encouraging results, even under extreme

682   conditions (high rain rate). For the wind direction, the amplitude of the azimuthal

683   modulation in the active mode decreases with increasing wind speed, while it increases

684   for the passive measurements. This also favours the use of WindSat for the estimation of

685   the direction of high winds. However, given the limited amplitude of the signals, a good

686   instrument accuracy has to be achieved (of the order of 0.2 K) to retrieve accurate wind

687   direction from the polarimetric measurements (English et al., 2006). We only briefly

688   tested the joint use of passive and active mode for wind speed retrieval. This possibility

689   should be examined further, to benefit from the different sensitivity of the two modes to

690   the various wind speed ranges.

691   The main problem for the development of retrieval methods adapted to high wind

692   speed lies in the lack of wind references under extreme conditions. This implies the need

693   to develop dedicated collocated database. This also encourages the use of sea state

694   information to trace efficiently the resulting scattered large swell conditions from

695   localized extreme conditions, to better analyze extreme events intensity.

696

705

706

707

708

709

710

711

712 **References**

713 Adams, I. S., C. C. Henneon, W. L. Jones, and K. A. Ahamad (2006), Evaluation of

714   hurricane ocean vector winds from WindSat, *IEEE Trans. Geo. Sc. Remote Sens., 44,*

715   656-667.

716 Bettenhausen, M. H., G. K. Smith, R. M. Bevilacqua, N.-Y. Wang, P. W. Gaiser, and S.

717   Cox (2006), A nonlinear optimization algorithm for WindSat wind vector retrievals,

718   *IEEE Trans. Geo. Sc. Remote Sens., 44*, 597-610.

719 Brown, S. T., C. S. Ruf, and D. R. Lyzenga (2006), An emisisvity-based wind vector

720   retrieval algorithm for the WindSat polarimetric radiometer", *IEEE Trans. Geo. Sc.*

721   *Remote Sens., 44*, 611-621.

722 Coppo, P., J.T. Johnson, L. Guerriero, J.A. Kong, G. Macelloni, F. Marzano, P.

723   Pampaloni, N. Pierdica, D. Solimini, C. Susini, G. Tofani, and Y. Zhang (1996),

724   Polarimetry for passive remote sensing, ESA contract 1146/95/NL/NB, Final report.

725 Deblonde, G. (2000), Evaluation of FASTEM and FASTEM-2, *NWP SAF Report*,

726   http://www.metoffice.com/research/interproj/nwpsaf/rtm/.

727 Ellison, W., A. Balana, G. Delbos, K. Lamkaouchi, L. Eymard, C. Guillou, and C.

728   Prigent (1998), New permittivity measurements and interpolation functions for natural

729   sea water, *Radio Sc., 33*, 668-685.

730 English, S. J., and T.J. Hewison (1998), A fast generic millimetre wave emissivity

731   model, *Microwave Remote Sensing of the Atmosphere and Environment Proc. SPIE*

732   3503, 22-30.

733 English, S., B. Candy, A. Jupp, D. Beddington, S. Smith, and A. Holt (2006), An

734   evaluation of the potential of polarimetric radiometry for numerical weather prediction

735   using QuikSCAT, *IEEE Trans. Geo. Sc. Remote Sens.*, *44*, 668-675.

736 Eyre, J. R. (1991), A fast radiative transfer model for satellite sounding systems,

737   *ECMWF Research Dept. Tech. Memo.176* (available from the librarian at ECMWF).

738 Fernandez, D. E., J. R. Carswell, S. Frasier, P. S. Chang, P. G. Black, and F. D. Marks

739   (2006), Dual-polarized C- and Ku-band ocean backscatter response to hurricane-force

740   winds, *J. Geophys. Res., 111*, C08013, doi:10.1029/2005JC003048.

741 Freilich, M. H., and B. A. Vanhoff (2006), The accuracy of preliminary WindSat vector

742   wind measurements: Comparisons with NDBC buoys and QuikSCAT, *IEEE Trans.*

743   *Geo. Sc. Remote Sens.*, *44*, 622-637.

744 Gaiser, P. W., K.M. St Germain, E.M. Twarog, G.A. Poe, W. Purdy, D. Richardson, W.

745   Grossman, W.L. Jones, D. Spencer, G. Golba, J. Cleveland, L. Choy, R.M.

746 Bevilacqua, P.S. Chang (2004), The WindSat spaceborne polarimetric microwave

747   radiometer: Sensor description and early orbit performance, *IEEE Trans. Geo. Sc.*

748   *Remote Sens.*, *42*, 2347-2361.

749 Huddelston, J. N., and B. W. Stiles (2000), Multidimensional histogram (MUDH) rain

750   flag, *Jet Propulsion Laboratory, California Institute of Technology*.

751 Kudryavtsev, V., and J. Johannessen (2004), Effect of wavebreaking on spectrum of

752   short wind waves, *Geophys. Res. Let.*, *31*, L20310.

753 Kudryavtsev V., D. Hauser, G. Caudal, and B. Chapron (2003), Semi-empirical model

754   of the normalized radar cross-section of the sea surface. 1. Background model, *J.*

755   *Geophys. Res.*, *108*, 8054, doi: 10.1029/2001JC001003.

756   Liu, Q., and F. Weng (2002), A microwave polarimetric two-stream radiative transfer

757   model, *J. Atmos. Sci*., *59*, 2396-2402.

758   Liu, Q., and F. Weng (2003), Retrieval of sea surface wind vectors from simulated

759   satellite microwave polarimetric measurements, *Radio Sc*., *38*, 8078,

760   doi:10.1029/2002RS002729.

761   Matricardi, M., F. Chevallier, G. Kelly, and J.N. Thépaut (2004), An improved general

762   fast radiative transfer model for the assimilation of radiance observations, *Quat. J.*

763   *Roy. Meteor. Soc., 130,* 153-173.

764   Mears C. (2000), Sea Winds on QuikSCAT normalized objective function rain flag,

765   version 1.2, 13pp, Remote Sensing System*,* Santa Rosa, Calif.

766   Monahan, E. C., and I. O Muircheartaigh (1986), Whitecaps and the passive remote

767   sensing of the ocean surface, *Int. J. Remote Sensing*, *7*, 627-642.

768   Monaldo, F. M. (2006), Evaluation of WindSat wind vector performance with respect to

769   QuikSCAT estimates, *IEEE Trans. Geo. Sc. Remote Sens*., *44*, 638-644.

770   Mouche, A., B. Chapron, and N. Reul (2007a), Asymptotic theory for ocean surface

771   electromagnetic waves scattering, in press in *Waves in Random and Complex Media*.

772   Mouche, A., B. Chapron, N. Reul, D. Hauser, and Y. Quilfen (2007b), Importance of the

773   sea surface curvature to interpret the normalized radar cross-section, submitted to *J.*

774   *Geophys. Res*.

775   Powell, M. D., P. J. Vickery, and T. A. Reinhold (2003), Reduced drag coefficient for

776   high wind speeds in tropical cyclones, *Nature*, *422*, 279-283.

777   Quilfen, Y., B. Chapron, T. Elfouhaily, K. B. Katsaros, and J. Tournadre (1998),

778   Observations of tropical cyclones by high-resolution scatterometry, *J. Geophys. Res.*,

779   *103*, 7767–7786.

780   Quilfen, Y., B. Chapron, A. Bentamy, J. Gourrion, T. Elfouhaily, and D. Vandemark

781   (1999), Global ERS-1/2 and NSCAT observations: upwind/downwind and

782   upwind/crosswind measurements. *J. Geophys. Res.*, *104*, 11459-11469.

783   Quilfen, Y., J. Tournadre, and B. Chapron (2006), Altimeter dual-frequency

784   observations of surface winds, waves, and rain rate in tropical cyclone Isabel, *J.*

785   *Geophys. Res.*, *111*, C01004, doi:10.1029/2005JC003068.

786   Reul, N., and B. Chapron (2003), A model of sea-foam thickness distribution for

787   passive microwave remote sensing applications, *J. Geophys. Res., 108*, C10, 3321,

788   doi:10.1029/2003JC001887.

789   Rose, L.A., W.E. Asher, S.C. Reising, P.W. Gaiser, K.M. St Germain, D.J. Dowgiallo,

790   K.A. Horgan, G. Farquharson, and E.J. Knapp (2002), Radiometric Measurements of

791   the Microwave Emissivity of Foam. *Trans. Geosci. Rem. Sens., 40*, 2619-2625.

792   Tournadre, J., and Y. Quilfen (2003), Impact of rain cell on scatterometer data: 1.

793   Theory and modelling. *J. Geophys. Res.*, *108*, C7, 3225, doi:10.1029/2002JC001428.

794   Tournadre, J., and Y. Quilfen (2005), Impact of rain cell on scatterometer data: 2.

795   Correction of Seawinds measured backscatter and wind and rain flagging, *J. Geophys.*

796   *Res.*, *110*, C07023, doi:10.1029/2004JC002766.

797   Yueh, S. H., W. J. Wilson, S. J. Dinardo, and S. V. Hsiao (2006), Polarimetric

798   microwave wind radiometer model function and retrieval testing for WindSat, *Trans.*

799   *Geo. Sc. Remote Sens.*, *44*, 585-595.

800   WindSat Data Products User's Manual, Version 3.0 (2006), D-29825, Ted Lungu

801   Editor.

802

803

804

805

	rms (no rain)	mean (no rain)	rms (rain)	mean (rain)	rms (ws>15m/s)	mean (ws>15m/s)
WindSat	1.56	-0.75	3.12	-1.54	2.98	-1.75
WindSat (minus 6GHz)	1.57	-0.75	3.21	-1.53	2.98	-1.71
WindSat (minus 6 and 10 GHz)	2.36	-1.25	3.62	-2.04	4.33	-3.06
WindSat + QuikSCAT	1.73	-0.83	3.00	-1.71	2.90	-1.89
Operational WindSat	2.26	-0.38	8.70	5.54	4.75	-0.49

806

807   Table 1: The performance of the inversion for the different observation combinations.

808   The results are first presented for the non-rainy cases (WindSat CLW < 0.2 mm), for the

809   rainy cases, and finally for the wind speeds above 15 m/s. Unit in m/s.

810

811

812

813

814

815

816
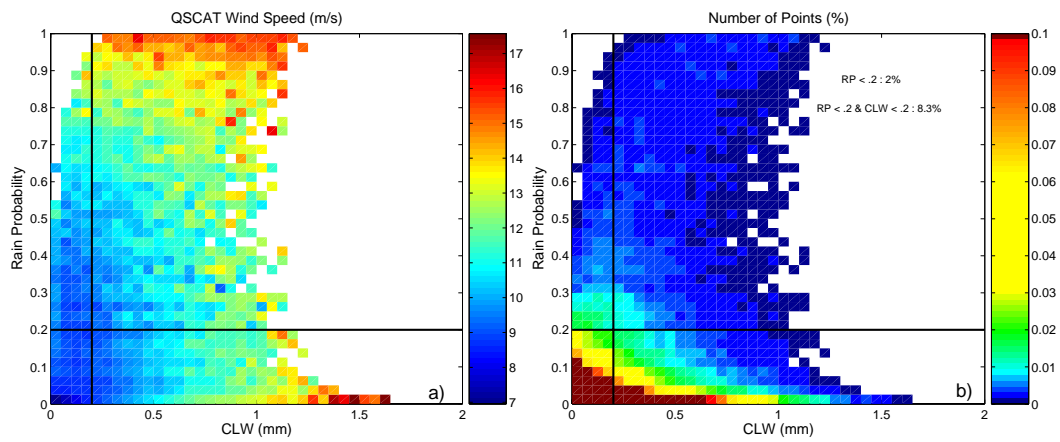
817

Figure 1: a) Mean QuikSCAT wind speed computed in RP / CLW bins and b) associated number of points, as a function of the rain probability (RP) and cloud liquid water content (CLW).

822

823

824

825

826

827

828

829

830

831

832

833
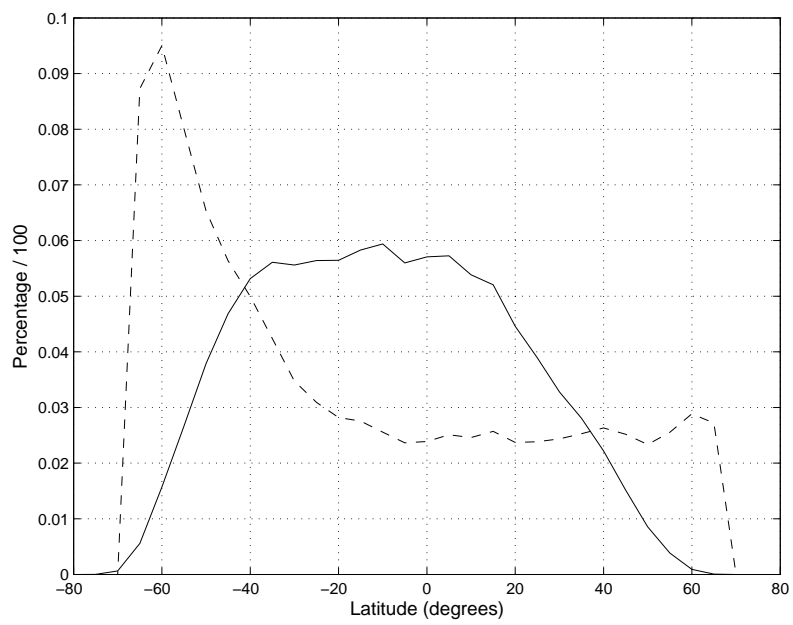
834

835

836

837 Figure 2: Distribution of the collocated WindSat / QuikSCAT (solid line) and WindSat /

838 Jason (dashed line) observations as a function of latitude.

839

840

841

842

843

844
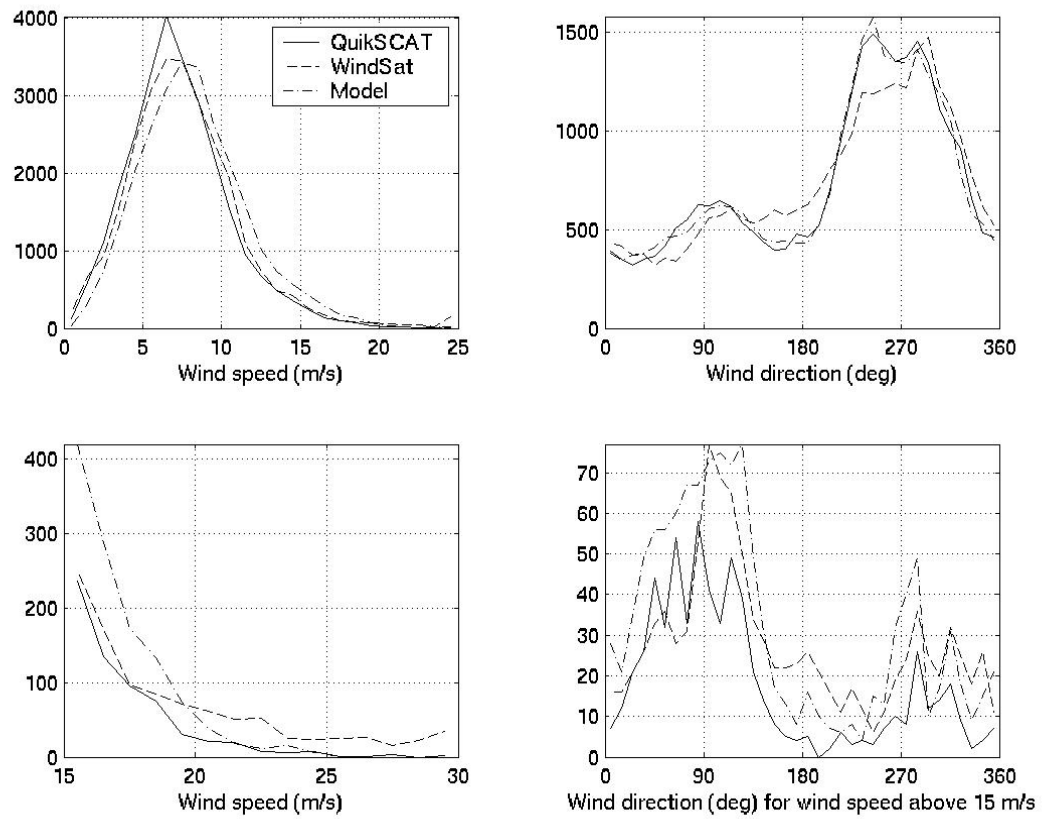
845

846   Figure 3: Distribution of the wind speeds from the collocated database. Histograms are

847   presented for QuikSCAT, WindSat, and the NCEP model estimates.

848

849

850

851

852

853

854

855

856
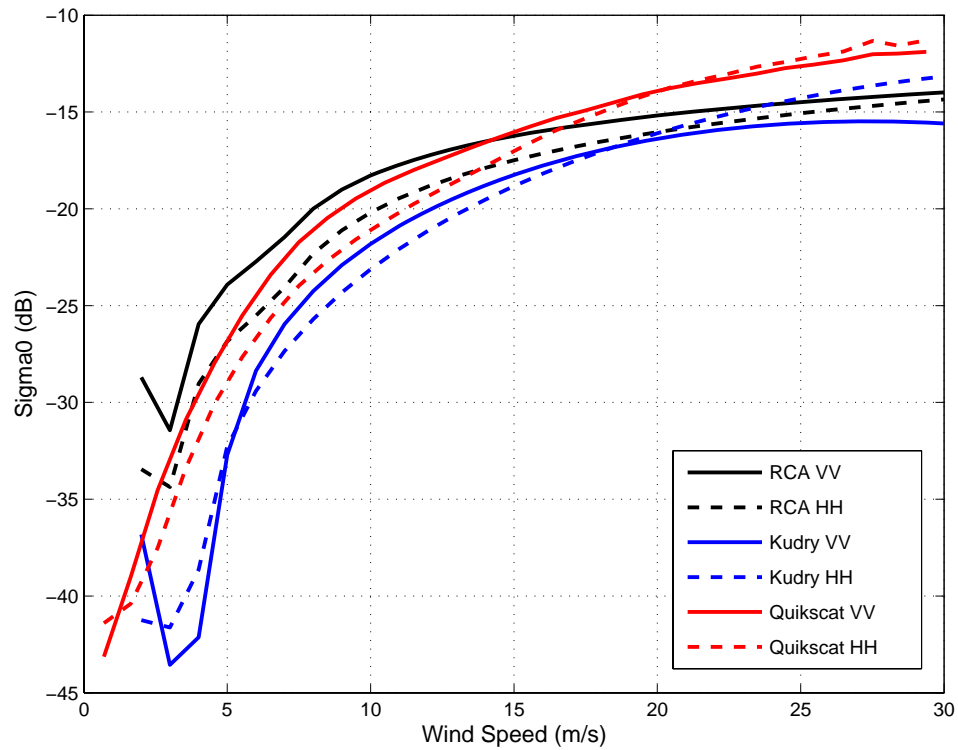
Figure 4: Mean Ku-band VV (solid lines) and HH (dashed lines) σ_0 (dB) computed with

the RCA model (black), the Kudryavtsev model (blue), and the QuikSCAT data (red), as

a function of wind speed (m/s).

860

861

862

863

864

865

866

867
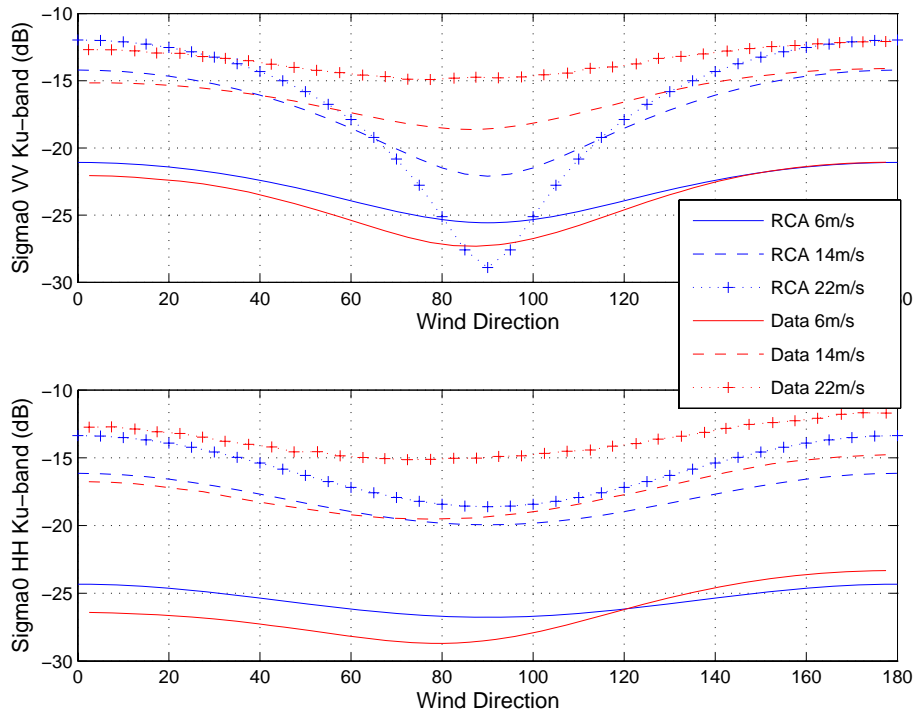
Figure 5: Mean Ku-band VV (top panel) and HH (bottom panel) σ_0 (dB) computed with

the RCA model (blue) and QuikSCAT data (red), as a function of the wind direction

(degrees), for 6 m/s (solid lines), 14 m/s (dashed lines), and 22 m/s (+) mean wind speed.

871

872

873

874

875

876
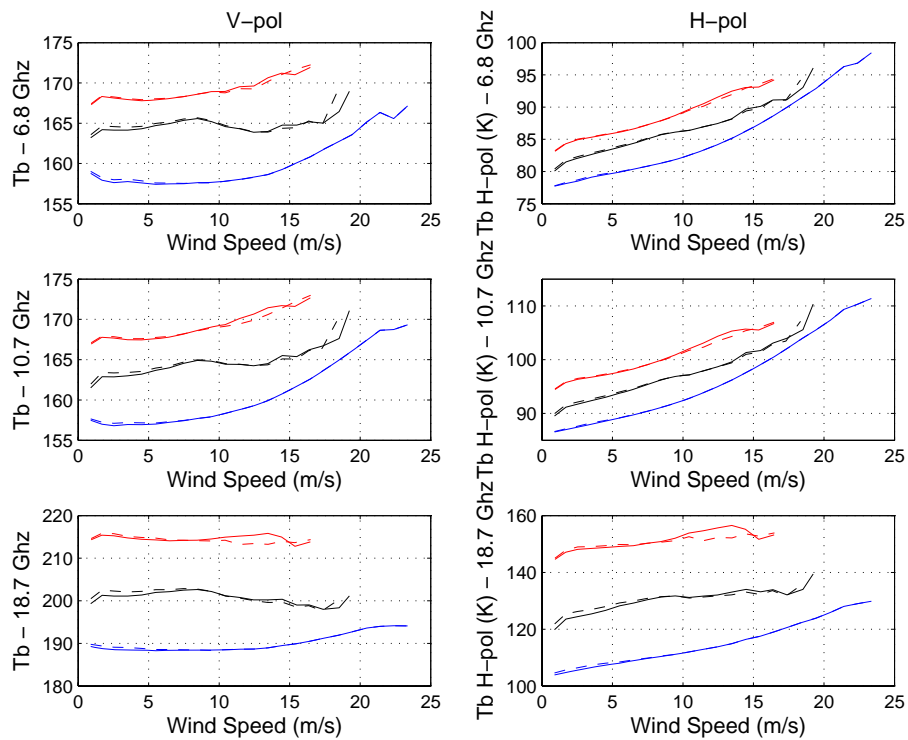
877

878

879

880 Figure 6: Mean V-pol (left panels) and H-pol (right panels) Tb's binned as a function of

881 ECMWF wind speed (m/s), at 6.8 GHz (top), 10.7 GHz (middle), and 18.7 GHz (bottom),

882 and for different integrated water vapor ranges: 0mm < WV < 20mm (blue lines), 20mm

883 < WV < 40mm (black lines), and 40mm < WV < 60mm (red lines). WindSat (dashed

884 lines) and Jason microwave radiometer (dashed lines) integrated water vapor data are

885 used.

886

887

888

889

890

891
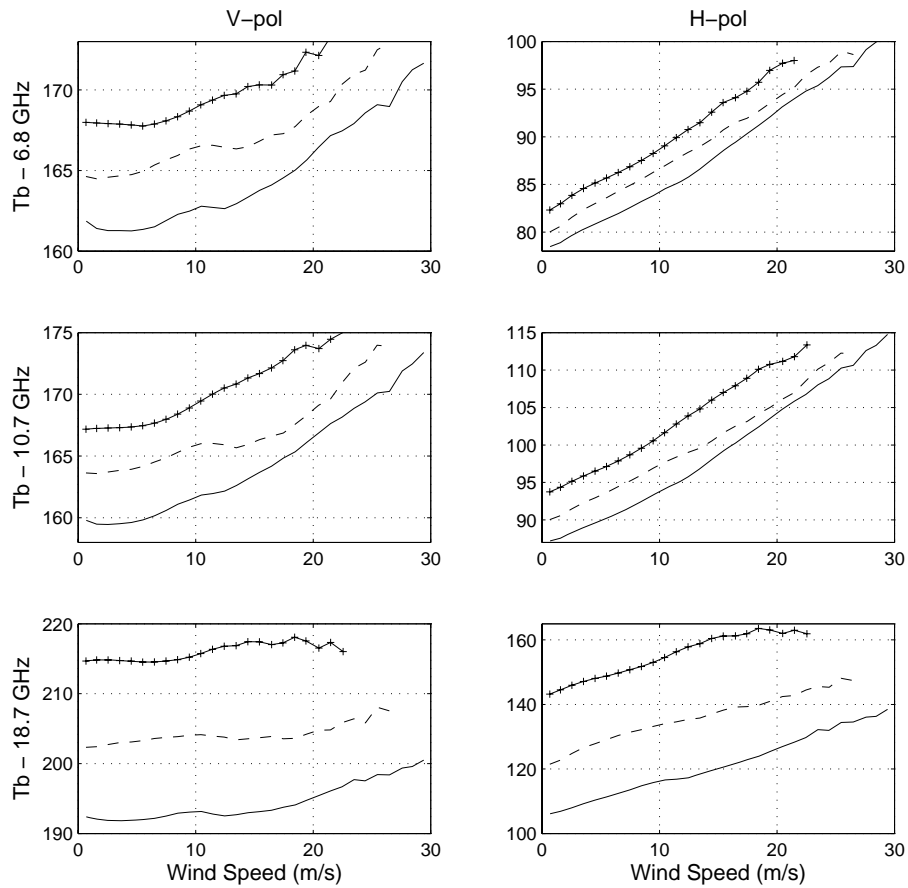
Figure 7: Mean V-pol (left panels) and H-pol (right panels) Tb's binned as a function of

QuikScat wind speed (m/s), at 6.8 GHz (top), 10.7 GHz (middle), and 18.7 GHz

(bottom), and for different integrated water vapor ranges: 0mm < WV < 20mm (solid

lines), 20mm < WV < 40mm (dashed lines), and 40mm < WV < 60mm (plus signs).

WindSat integrated water vapor data are used.

897

898

899

900

901

902

903

904
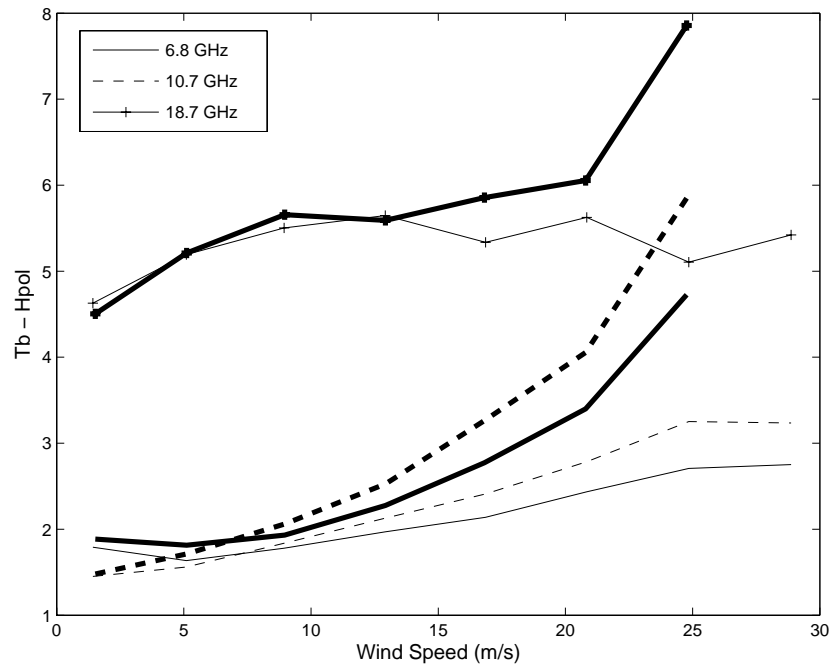
Figure 8: H-pol Tbs standard deviations binned as a function of QuikSCAT (thin lines)
and NCEP (thick lines) wind speed (2 m/s bins), at 6.8 GHz (solid lines), 10.7 GHz
(dashed lines), and 18.7 GHz (crosses). The integrated water vapor ranges is 0 mm < WV
< 20 mm.
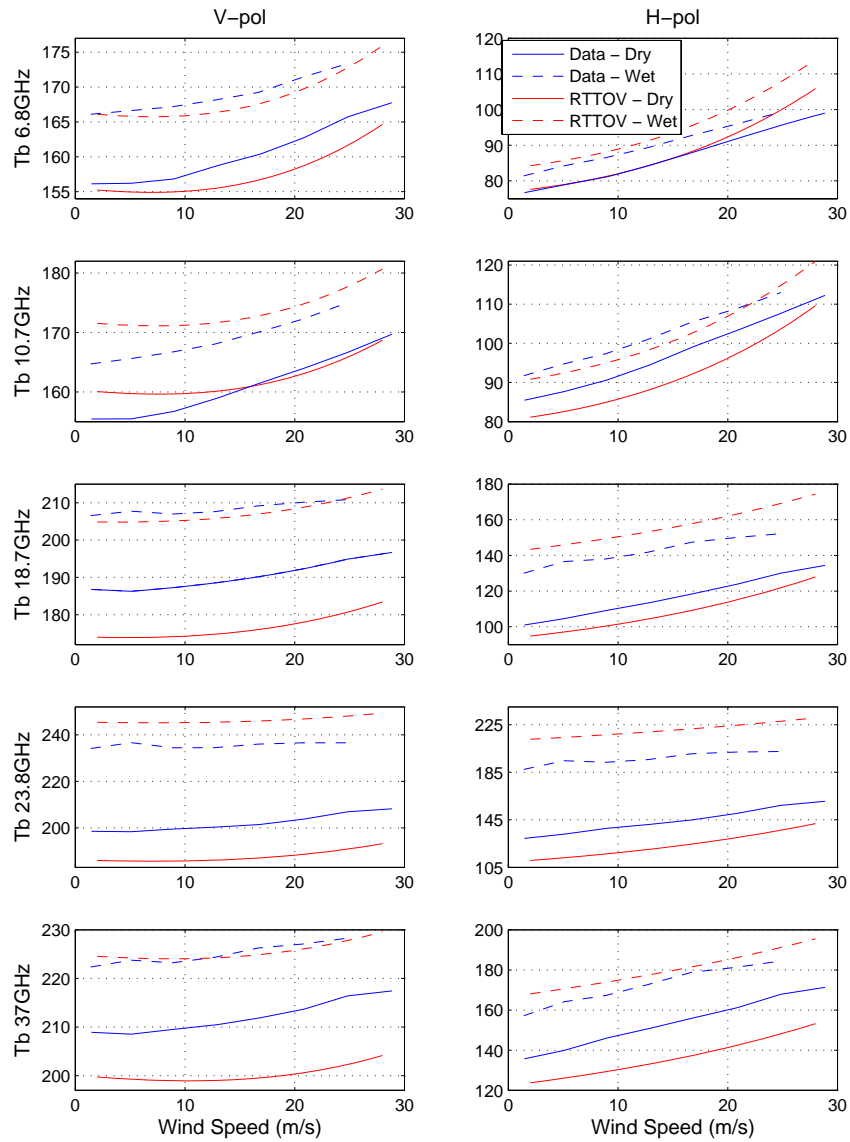
Figure 9: Mean V (left panels) and H (right panels) Tb's binned as a function of QuikSCAT wind speed (m/s), at 6.8 GHz, 10.7 GHz, 18.7 GHz, 23.8 GHz, and 37.0 GHz, respectively from top to bottom, for a dry atmosphere: 0 mm < WV < 20 mm (solid lines), and for a wet atmosphere 20 mm < WV < 60 mm (dashed lines). WindSat data are plotted as blue lines and RTTOV model as red lines.

916

917

918

919

920
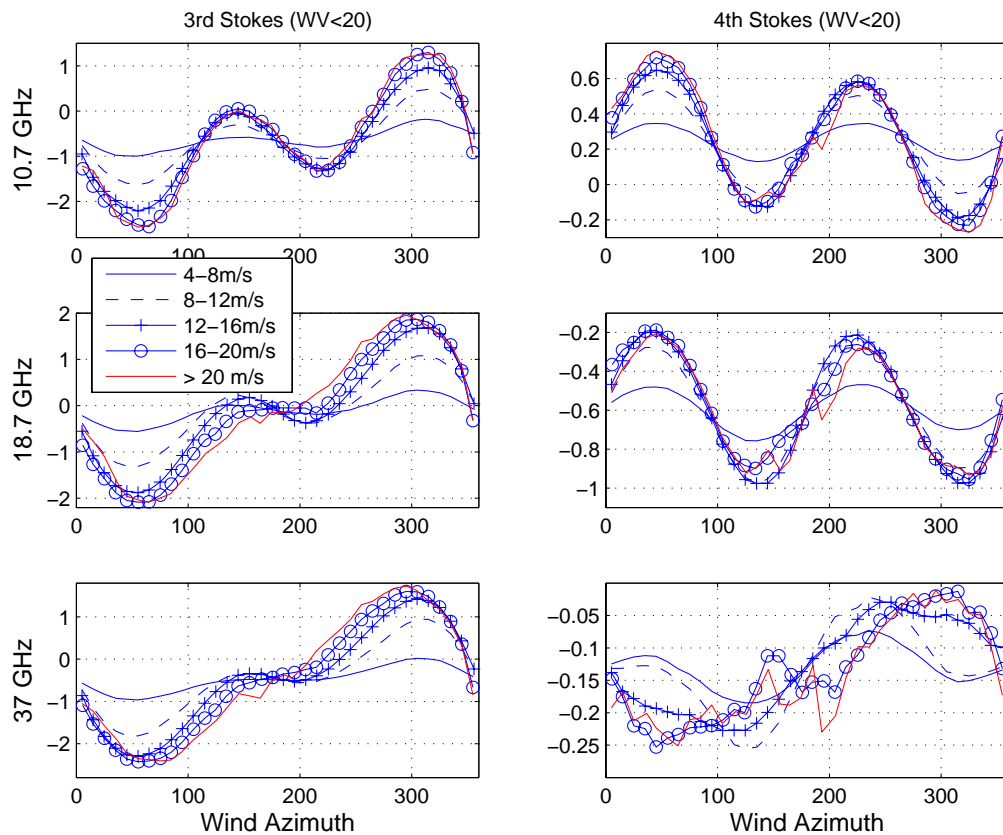
Figure 10: Mean 3rd (left panels) and 4th (right panels) Stokes parameters binned as a function of the relative wind direction (degrees), at 10.7 GHz (top), 18.7 GHz (middle), and 37.0 GHz (bottom), and for different wind speed ranges: 4 m/s < WS < 8 m/s (solid lines), 8 m/s < WS < 12 m/s (dashed lines), 12 m/s < WS < 16 m/s (+) , 16 m/s < WS < 20 m/s (o), WS > 20 m/s (red lines). Integrated water vapor is taken in the range WV < 20 mm.

927

928

929

930

931

932

933
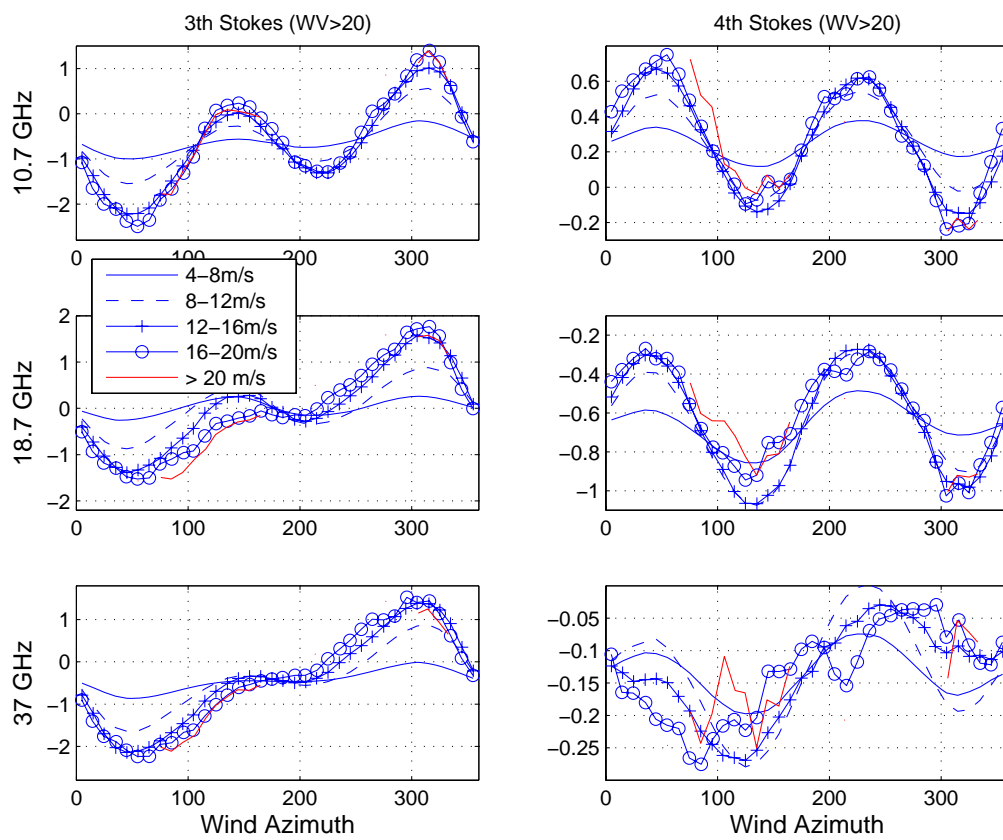
Figure 11: Same as Figure 10 with integrated water vapor taken in the range 20 mm <

WV < 50 mm.

936

937

938

939

940

941

942

943
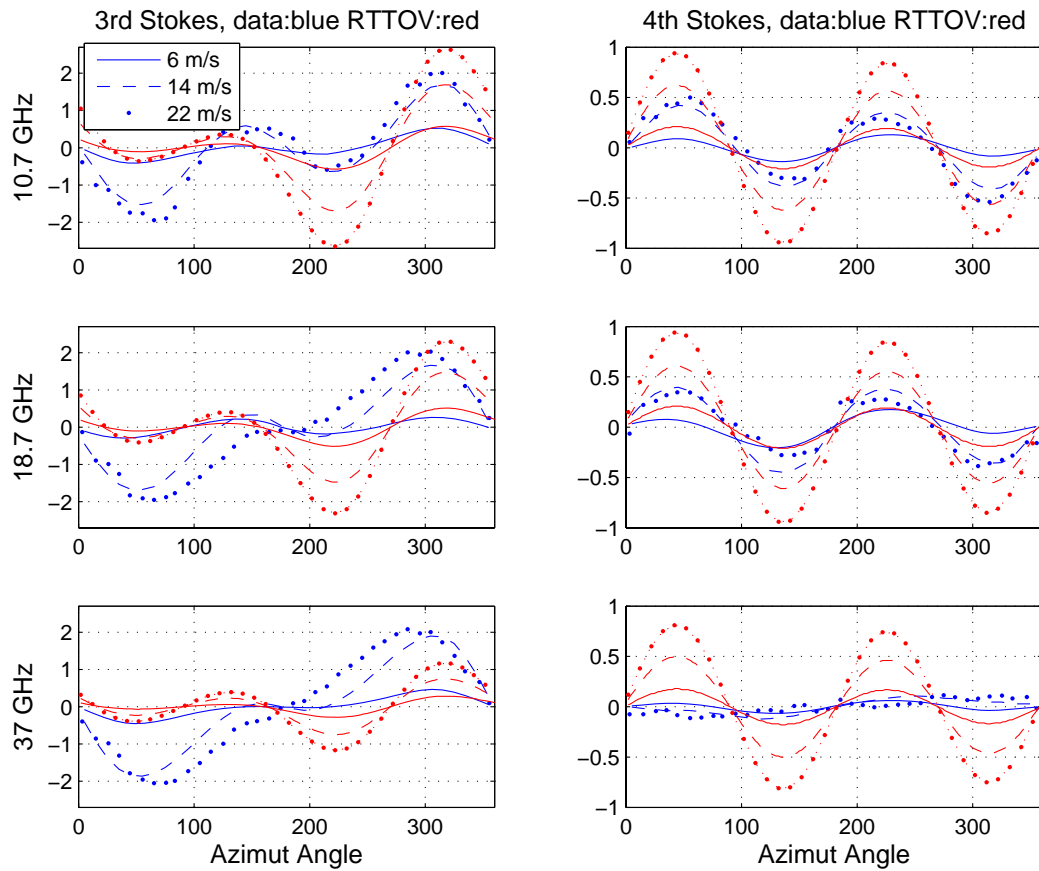
Figure 12: Mean 3rd (left panels) and 4th (right panels) Stokes parameters for WindSat (blue lines) and RTTOV-8 model (red lines) binned as a function of the relative wind direction (degrees), at 10.7 GHz (top), 18.7 GHz (middle), and 37.0 GHz (bottom), and for different wind speed ranges: 4 m/s < WS < 8 m/s (solid lines), 12 m/s < WS < 16 m/s (dashed lines), 20 m/s < WS < 24 m/s (dotted lines).

949

950

951

952

953

954

955

956
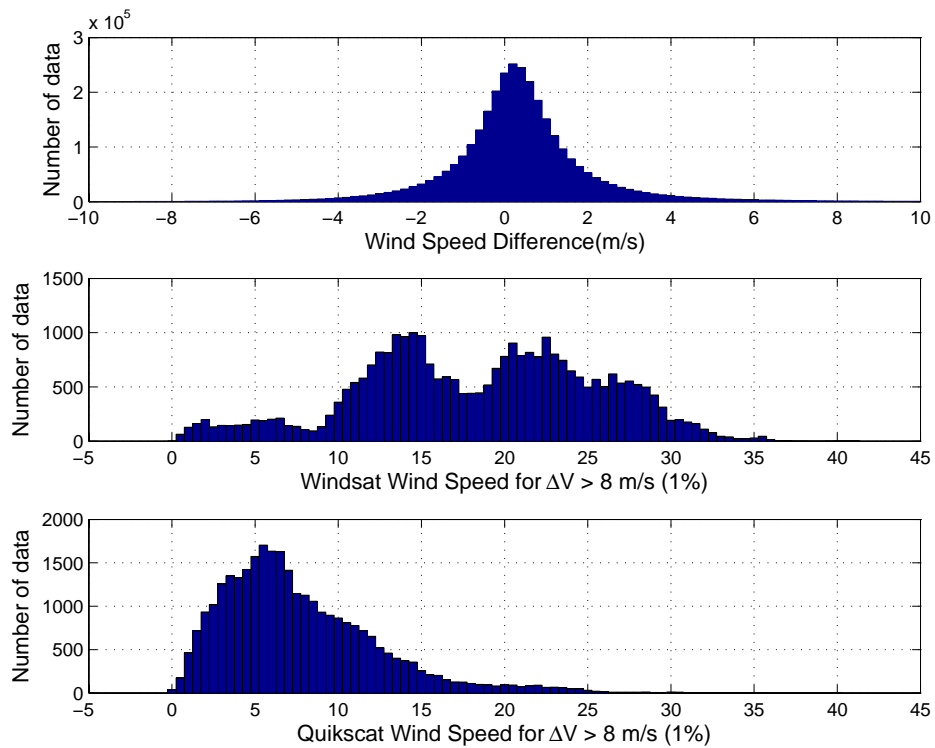
957

958

959 Figure 13: WindSat minus QuikSCAT wind speed difference distribution (top panel),

960 WindSat (middle panel) and QuikSCAT (bottom panel) wind speed distribution for wind

961 speed differences greater than 8 m/s.

962

963

964

965

966

967

968

969

970
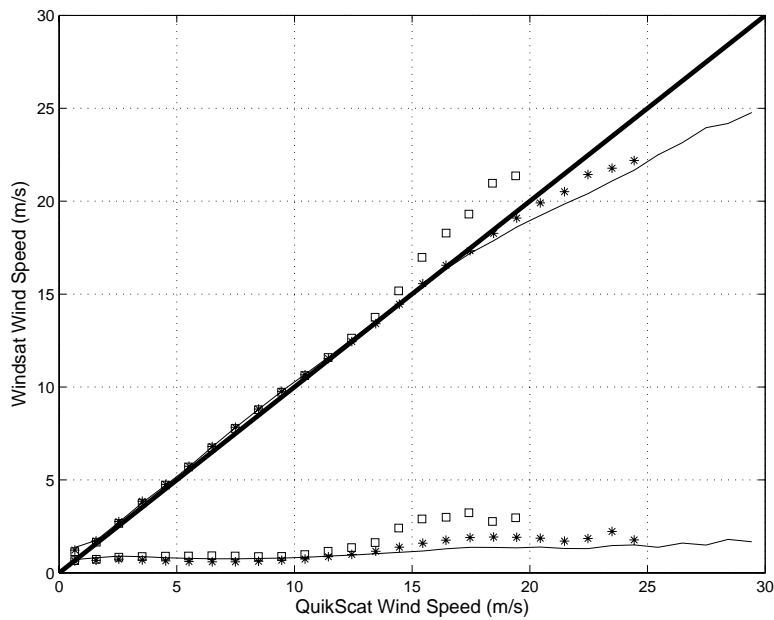
Figure 14: Mean WindSat speeds binned by QuikSCAT wind speeds, for 0 mm < WV <
20 mm (solid lines), 20 mm < WV < 40 mm (star), and 40 mm < WV < 80 mm (squares).
The thick solid line is the perfect fit line. The bottom curves display the standard
deviation of the WindSat minus QuikSCAT differences. WV stands for the WindSat
integrated water vapor content. Each bin contains at least 50 collocated measurements.
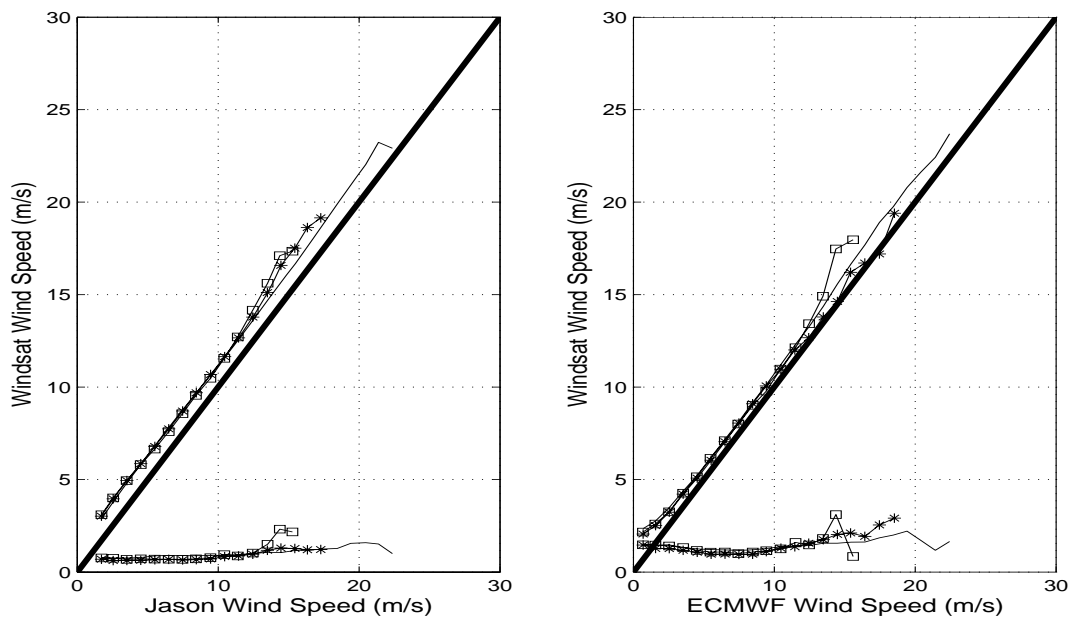
976

Figure 15: Mean WindSat speeds binned by Jason winds (left) and ECMWF winds (right), for 0 mm < WV <20 mm (solid lines), 20 mm < WV <40 mm (star signs), and 40 mm < WV < 80 mm (square signs). The thick solid line is the perfect fit line. The bottom curves display the standard deviation of the WindSat minus Jason (left) and ECMWF (right) differences. WV is retrieved from the Jason JMR radiometer. Each bin contains at least 20 points.
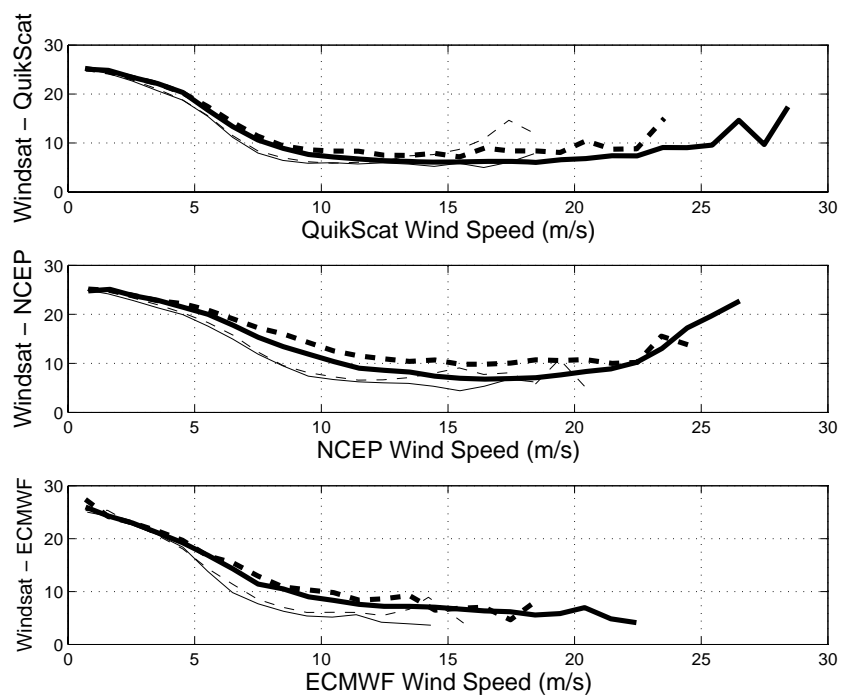
992

993

994

995

996

997

998

999

1000

1001 Figure 16: Standard deviation (degrees) of the WindSat wind direction minus QuikSCAT

1002 (top panel), NCEP (middle panel), ECMWF (bottom panel) wind direction, as a function

1003 of wind speed in tropical (thin lines) and mid-latitude areas (thick lines). WV ranges are 0

1004 mm < WV < 20 mm (solid lines) and 20 mm < WV < 80 mm (dashed lines). A minimum

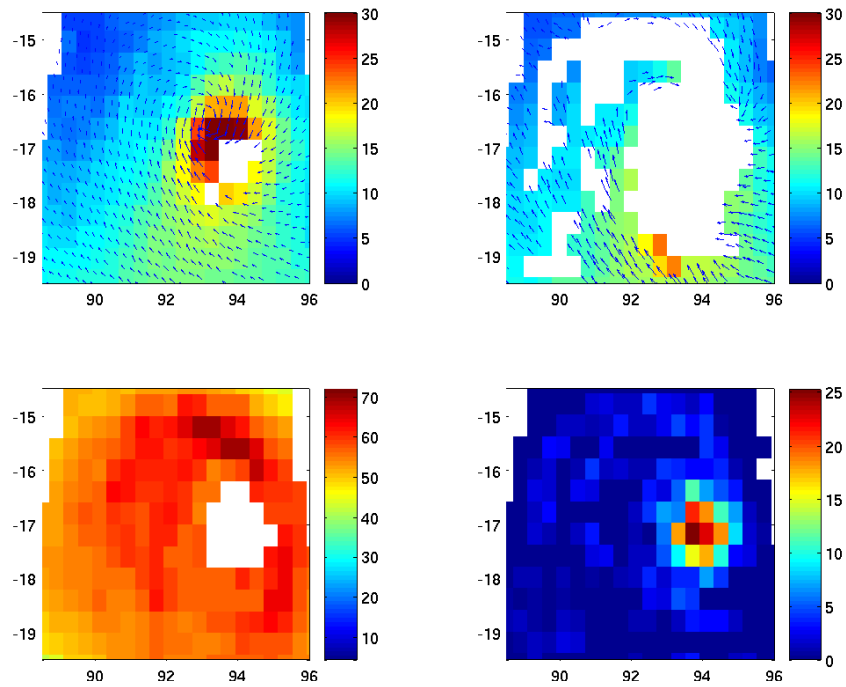1005 of 50 data points is required in each 1 m/s bin.

1013

Figure 17: QuikSCAT (top left) and WindSat (top right) wind fields, speed in m/s, for non rainy areas, in a tropical storm, February 10, 2003, 12h00 UTC. WindSat integrated water vapor content (bottom left in mm) and rain rate (bottom right in mm/hr).
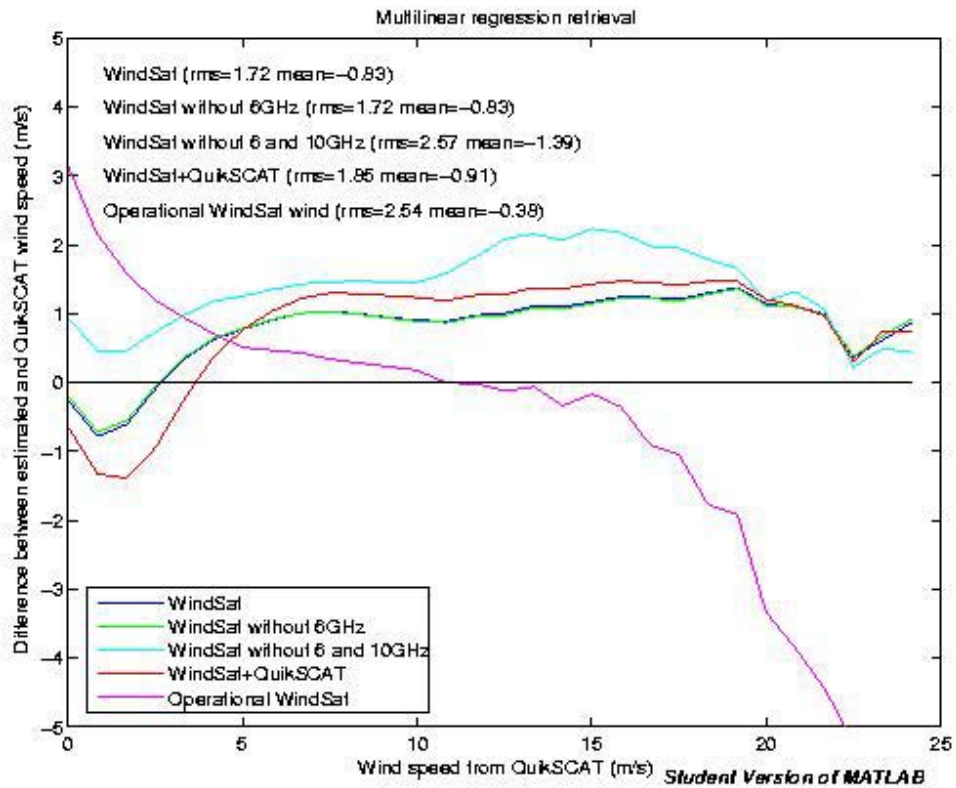
1017

1018

1019

1020

1021

1022

1023

Figure 18: Wind speed errors for different combinations of observations, stratified by the QuikSCAT wind speed taken as a reference. For each combination, the rms and mean errors calculated over the original data set (including rainy pixels) are indicated.